ACS Electrochemistry

pubs.acs.org/electrochem

Article

Impact of Interposer Microstructure on Ionic Transport in Liquid-Phase Bicarbonate Electrolysis

Elizabeth Dentzer, Hanwoong Kim, Yaguang Zhu, Hakhyeon Song, Nicole Callen, Claudio A. Ruiz Torres, Hyeonuk Choi, Jihun Oh, Marta C. Hatzell,* and Kelsey B. Hatzell*

Cite This: *ACS Electrochem.* 2026, 2, 1304–1312

Read Online

ACCESS | Metrics & More | Article Recommendations | Supporting Information

ABSTRACT: The electrochemical reduction of CO_2 (CO_2RR) is a potentially scalable approach for converting captured carbon dioxide into value-added products. Conventional gas-phase electrolysis systems can suffer from carbonate crossover, which limits the efficiency of the system. Liquid-phase (bi)carbonate electrolysis using bipolar membrane electrode assemblies (BPM-MEA) has emerged as a promising alternative. The interposer layer, a porous mass-transport material between the BPM and the catalyst, is an essential component of the MEA, as it allows evolved CO_2 to reach the catalyst surface for reaction. In the absence of this layer, evolved CO_2 generated by the pH swing process at the BPM can be converted back into (bi)carbonate (CO_2 recapture) due to the high bulk pH. Thus, clear design guidelines are needed to maximize CO_2 conversion, minimize CO_2 recapture in the catholyte, and improve energy efficiency. Here, the transport properties of the interposer are systematically characterized by X-ray tomography and symmetric-cell impedance spectroscopy to quantify porosity, tortuosity, and the resulting MacMullin number. We then examine the correlation between these material properties and the electrolyzer performance. We focus on characterizing two commercial porous membrane filters, mixed cellulose ester (MCE) and poly(ether sulfone) (PES).

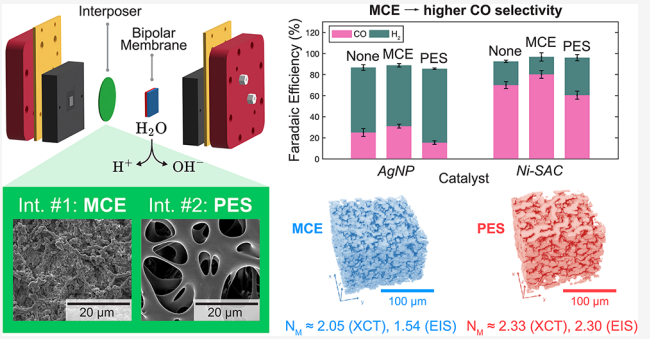

KEYWORDS: *CO_2 electrolysis, bipolar membrane electrolyzer, tomography porous interposer, liquid-phase electrolysis*

INTRODUCTION

Atmospheric CO_2 concentrations surpassed 420 ppm in 2024, intensifying the urgency to deploy negative-emission technologies that capture and upgrade carbon into value-added products.[1] While most captured CO_2 is injected for enhanced oil recovery or geological sequestration, several chemical pathways enable utilization into fuels and chemicals, including sustainable aviation fuels, organic carbonates, methanol, urea, and aliphatic or olefinic hydrocarbon chains.[2−4]

Gas-phase anion-exchange membrane (AEM) electrolyzers can reduce CO_2 to syngas (CO + H_2), but suffer from low carbon utilization because significant CO_2 crosses over to the anode.[5−7] As a result of this crossover, AEM systems require energy-intensive regeneration steps to re-liberate CO_2 gas from bicarbonate using thermal or acid−based processes. In addition, CO_2 regenerated at the anode must also be separated from O_2. Integrated carbon capture and conversion systems with bipolar membrane (BPM) electrolysis offer a more efficient alternative to AEM electrolyzers. In one step, these systems convert aqueous (bi)carbonate into syngas or pure CO, which can be upgraded to more valuable liquid products.[8,9] This eliminates the need for CO_2 re-liberation, reduces carbon losses, and avoids additional thermal units, such as calciners, slakers, and pellet reactors, that are inherent to AEM systems.[4,10,11] BPM reactors thus not only improve efficiency but also reduce the energy consumption of the carbon capture system.[12,13]

Recently, numerous research groups have conducted comprehensive studies on (bi)carbonate electrolysis in the BPM−MEA systems.[14,15] Significant efforts have focused on tailoring the Ag- and Cu-based catalyst and electrode assemblies to steer selectivity.[3,9,12,13,16] Trends in catalyst design for BPM bicarbonate electrolyzers should mirror trends seen in AEM CO_2 electrolyzers, as both systems reduce gas-phase CO_2 in an alkaline environment. However, the systems differ in the local reaction environment near the catalyst, with bicarbonate systems having lower gas-phase CO_2 concentrations, higher HCO_3^- concentrations, and a more variable pH gradient.

Received: January 28, 2026
Revised: March 31, 2026
Accepted: April 7, 2026
Published: April 14, 2026

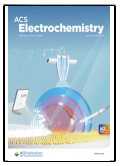

These changes in mass concentration at the catalyst surface are due to CO_2 being generated within the reactor rather than supplied. CO_2 is generated through a pH swing process initiated by the water dissociation within the BPM. The protons generated by the BPM react immediately with bicarbonate (HCO_3^-) ions in the catholyte, producing dissolved CO_2 and water.[17,18] The dissolved CO_2 must then be transported to the catalyst for the reaction to proceed.[19,20] In principle, this process provides a steady local supply of CO_2 from the bicarbonate reservoir, helping buffer the catalyst against CO_2 starvation.

However, this is not always the case, as in some systems the transport distance for dissolved CO_2 is too long, and the CO_2 can then react first with the electrolyte and be converted back into bicarbonate. Due to these differences in electrolyte composition and catalyst reaction environment, significant effort has been devoted to understanding and tuning proton, CO_2, and HCO_3^- mass transport between the bipolar membrane and the catalyst surface through the design of interposer layers.[3,13,21,22]

BPM electrolysis faces two main transport challenges: (i) insufficient CO_2 liberation *in situ* from bicarbonate and (ii) rapid CO_2 recapture back into (bi)carbonate, both of which limit CO_2 availability at the cathode.[21,23,24] In reverse-bias BPM bicarbonate electrolysis, water dissociation at the bipolar junction generates H^+ at the cathode-facing CEM interface and OH^- at the anode-facing AEM interface. These protons react with bicarbonate species to produce CO_2 locally within the interposer region. A porous interposer layer inserted between the BPM and the catalyst layer spatially separates the highly acidic region near the BPM from the more alkaline electrolyte environment near the catalyst surface, establishing a local pH gradient within the porous structure. This region is where protons from the BPM encounter bicarbonate ions, determining where CO2 is regenerated and how effectively it reaches the catalyst.[25] Without an interposer, protons can directly contact the catalyst surface, promoting hydrogen evolution and diminishing CO_2 selectivity. Additionally, without a defined porous microenvironment, *in situ* generated CO_2 may be rapidly recaptured as bicarbonate before reaching the catalyst. In this way, the interposer acts both as a physical spacer and as a transport-regulating interphase that mediates proton flux, CO_2 generation, ionic conduction, and reactant residence time.

An effective interposer must regulate the transport of both ionic species (bicarbonate, proton, hydroxide) and dissolved or gaseous CO_2 within the catholyte region. Here, we directly link interposer transport properties to electrochemical behavior by combining X-ray tomography and impedance spectroscopy to quantify the MacMullin number for two commercial interposers: mixed cellulose ester (MCE) and poly(ether sulfone) (PES). The MacMullin number quantifies the extent to which a porous material hinders ionic and electrical transport relative to the pure electrolyte.[26,27] The MacMullin number is a dimensionless parameter that relates the tortuosity of a porous medium to its porosity, linking bulk properties to those experienced under confinement or within porous structures. By comparing these structural and electrochemical measurements, we assess how interposer transport properties influence electrolyzer energy requirements and product selectivity. Together, these techniques clarify how interposer architecture shapes local ion and gas transport within the catholyte.

METHODS AND MATERIALS

Materials

For our interposers, we purchased mixed cellulose ester (MCE) and poly(ether sulfone) (PES) membrane filters from Sterlitech (Auburn, WA), each with a nominal pore size of 8 μm. 3 mm diameter CHI104 glassy carbon electrodes were obtained from CH Instruments (Austin, TX). The bipolar membrane (BPM) was supplied by Alfa Chemistry (Holbrook, NY). The catholyte and anolyte used were 1M potassium bicarbonate (KHO_3) and 1 M potassium hydroxide (KOH), respectively, both prepared with deionized water.

Ni-based single-atom catalyst (Ni-SAC) was synthesized as described in ref.10 Briefly, carbon black, 2-methylimidazole, and $Ni(NO_3)_2{\cdot}6H_2O$ were dispersed in ethanol and sonicated for 30 min. After removing the solvent using a rotary evaporator, the dried precursor powder was finely ground using a mortar and pestle. The ground powder was then calcinated at 800 °C in a tube furnace under argon flow. The final homogenous Ni-SAC catalyst was obtained by further grinding using a mortar and pestle.

The cathode was either a silver nanoparticle (AgNP)-coated or Ni-SAC-coated gas diffusion electrode (GDE). A catalyst ink was prepared by dispersing 200 mg of solid silver nanoparticles (200-400 nm) from MSE Supplies (Tucson, AZ) or synthesized Ni-SAC powder in 25 mL of ethanol along with 241 μL of 5% perfluorosulfonic acid (PFSA) ionomer solution from Fuel Cell Store (Bryan, TX). The suspension was bath-sonicated for 30 min before use. The ink was spray-coated onto a 20 cm^2 carbon paper substrate using a G233-SET-H Master Airbrush while the paper was held at a 45° incline on a hot plate maintained at 150 °C. This spraying process was repeated until the total catalyst loading reached 2 mg/cm^2. For each electrolysis experiment, a fresh 1 cm^2 square of the coated carbon paper was cut for use.

X-ray Tomography and Image-Based Tortuosity Analysis

For porous media, the MacMullin number is defined geometrically as the ratio of tortuosity to porosity, as shown in eq 1, where τ is the through-plane tortuosity and ε is the porosity of the pore network.

$$N_M = \frac{\tau}{\varepsilon} \tag{1}$$

Physically, the MacMullin number represents the increase in ionic transport resistance imposed by a porous medium relative to the bulk electrolyte. Higher tortuosity increases the effective path length for ion transport, and lower porosity reduces the available cross-sectional area for conduction. Together, these structural factors determine the transport penalty introduced by the porous material.

The MacMullin numbers of the two porous interposers explored in this work, PES and MCE, were determined using two independent approaches: (1) image-based structural analysis via X-ray computed tomography (XCT) to quantify tortuosity and porosity, and (2) electrochemical impedance spectroscopy (EIS) to determine the effective ionic conductivity of the interposers. This section describes the XCT-based approach used to determine the structural parameters appearing in eq 1.

Samples were imaged using an X-ray computed tomography system (Zeiss Xradia 630, Carl Zeiss X-ray Microscopy, Pleasanton, CA). Specimens were mounted on a low-attenuation holder and mechanically stabilized to minimize motion during acquisition.[28−30] Prior to scanning, source warm-up and system calibration were performed following the manufacturer's recommended procedures.

X-ray tomographic datasets of each separator material were processed to generate binarized representations of the pore structure. To segment the pore space, image thresholding was performed with threshold values selected based on porosity estimates obtained independently through an Archimedes-based gravimetric method. Interposer samples (MCE and PES) were first weighed dry, then re-weighed after being fully saturated in water, ethanol, and isopropanol. These solvents were chosen because of their compatibility with both membrane materials. The calculated porosity values were used to

https://doi.org/10.1021/acselectrochem.6c00038
ACS Electrochem. 2026, 2, 1304−1312

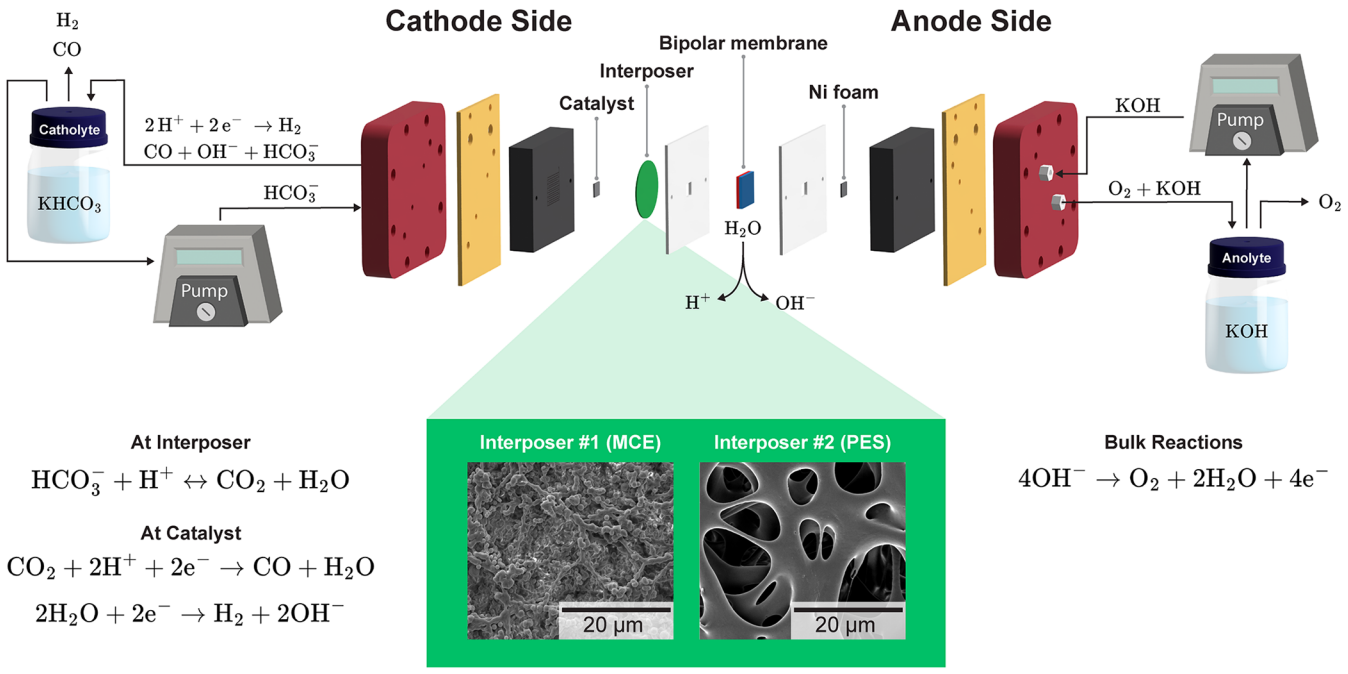

Figure 1. Top: Diagram of the catholyte and anolyte flow setup in a CO_2 electrolysis cell with a bipolar membrane (BPM), catalyst layer (AgNP or Ni-SAC), and a porous interposer (MCE or PES). KHO_3 catholyte is circulated to supply bicarbonate ions, which are *in situ* converted to CO_2 at the interposer interface. The BPM supplies H^+ and OH^- to enable CO and H_2 production at the cathode and O_2 evolution at the anode in KOH electrolyte. Bottom: Representative scanning electron microscopy (SEM) images of the two interposers used in this study: MCE (left) and PES (right), both with 8 μm nominal pore size.

validate the segmented pore volumes and help select an appropriate threshold level.

Pore size distributions (PSD) were determined from three representative sub-volumes from each tomographic dataset. A Euclidean distance transform followed by a local maxima detection was used to estimate local pore diameters from the binary images. Only pores resolvable at the imaging system's spatial resolution were included in the analysis.

The same three sub-volumes were processed using the TauFactor application in MATLAB to quantify tortuosity. The application simulates steady-state Fickian diffusion through the segmented porous medium, and simulations are performed along the primary axis of fluid flow to reflect transport conditions. The resulting porosity and tortuosity values were then used to calculate the MacMullin number for MCE and PES according to eq 1.

Electrochemical Impedance Spectroscopy in Swagelok Cell

While the MacMullin number can be expressed geometrically in terms of tortuosity and porosity, it can also be defined electrochemically as the ratio of the ionic conductivity of the bulk electrolyte to the effective ionic conductivity of the porous medium, as shown in eq 2.

$$N_M = \frac{\kappa_{BULK}}{\kappa_{INT}} \tag{2}$$

Physically, this definition reflects the increase in ionic transport resistance imposed by the porous interposer relative to the bulk electrolyte. A higher MacMullin number indicates that the porous structure more significantly impedes ionic conduction compared to the unobstructed electrolyte.

To determine the effective ionic conductivity of the interposers, electrochemical impedance spectroscopy (EIS) measurements were performed in symmetric Swagelok cells. Cells were assembled using two glassy carbon working electrodes separated by stacked interposer layers (either PES or MCE). Prior to assembly, interposers were pre-soaked in 1M KHO_3 for 15 min to ensure full wetting, and once assembled, the cell was flooded with 1M KHO_3. Electrochemical Impedance Spectroscopy (EIS) measurements were performed with a BioLogic SP-300 potentiostat at open-circuit potential (0 V vs OCP) over a frequency range of 200 kHz to 0.5 Hz using a 10 mV sinusoidal perturbation amplitude.

The separator stacking method was used to determine the intrinsic ionic resistance of the porous interposers. This approach is well established for determining the transport properties of porous separators and electrolytes.[27,31,32] Impedance measurements are performed in symmetric cells containing increasing numbers of electrolyte-filled separator layers, and the total measured resistance is plotted as a function of the number of layers. The slope of the resulting linear relationship gives the resistance of a single separator layer. For each interposer material, Swagelok cells were assembled with 1, 2, 3, 6, or 9 stacked interposer layers. For each assembled stack, EIS was measured three times for reproducibility, after which the cell was disassembled and reassembled for the next layer count. The total resistance of each stack (R_1) was determined from the high-frequency intercept of each Nyquist plot by fitting this region to a linear model and extracting the x-intercept. In this frequency regime, the impedance response is dominated by purely ohmic ionic transport through the electrolyte and interposer, while capacitive contributions from interfacial double-layer charging occur at lower frequencies and therefore do not influence the extracted resistance. A linear regression of R_1 versus the number of layers was used to extract the resistance of a single interposer, R_{INT}, from the slope (Figure S2).

Following EIS measurements, the total wet stack thickness was measured using a Mitutoyo Digimatic MDC-Lite micrometer (293-831-30; ±2 μm accuracy) for each layer count (1, 2, 3, 6, and 9). The thickness of a single interposer was determined from the slope of stack thickness versus layer number. Stacking multiple interposer layers was used only in this method to improve the accuracy of the resistance measurement by increasing the total transport path length, allowing the resistance of a single interposer to be extracted from the linear relationship between total resistance and layer number. The effective ionic conductivity (κ_{INT}) was then calculated from the resistance of a single interposer (R_{INT}), interposer thickness (t), and electrode area (A), as shown in eq 3.

https://doi.org/10.1021/acselectrochem.6c00038
ACS Electrochem. 2026, 2, 1304−1312

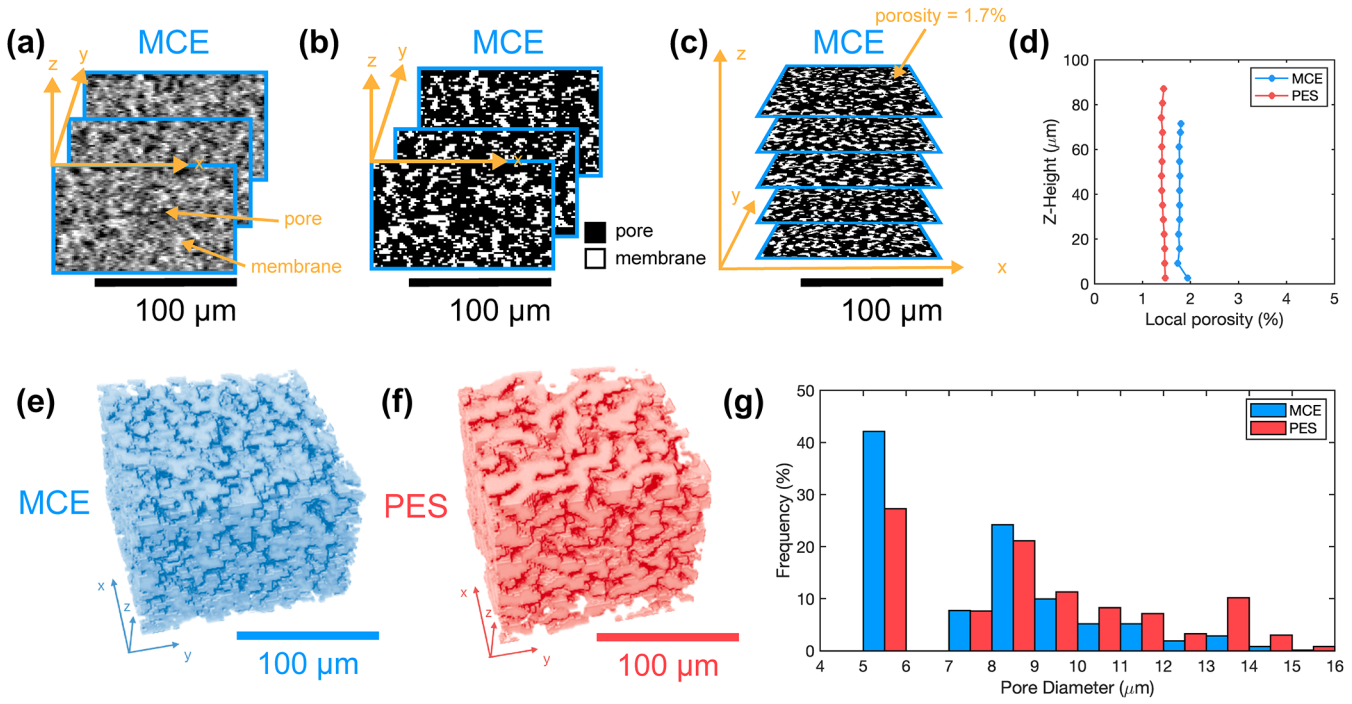

Figure 2. (a–c) Tomography image processing workflow for the MCE interposer, showing raw reconstructed slices (a), binarized pore segmentation (b), and stacked segmented volumes used for local porosity analysis (c). (d) Local through-plane porosity profiles of MCE and PES. (e, f) 3D renderings of the pore networks for MCE (e) and PES (f) interposers obtained from X-ray microtomography. (g) Pore size distributions derived from X-ray tomography (frequency-normalized, 1 bins).

$$\kappa_{INT} = \frac{t}{R_{INT} \cdot A} \tag{3}$$

The bulk electrolyte conductivity (κ_{BULK}) was measured using a calibrated benchtop conductivity meter (Orion Versa Star Pro). The MacMullin number for each interposer was then calculated using eq 2.

Electrolysis Experiments

Cell voltage and faradaic efficiency measurements were collected simultaneously during galvanostatic CO_2 electrolysis experiments using a zero-gap MEA cell. As shown in Figure 1, the cell contains either a bipolar membrane or a bipolar membrane with an interposer, a silver nanoparticle- or Ni-SAC-coated gas diffusion cathode, and a nickel foam anode. In this zero-gap configuration, the catalyst layer directly contacts either the bipolar membrane (no interposer condition) or a single interposer layer (when present).

The system was operated in a two-electrode configuration using a BioLogic SP-300 potentiostat, with a working and counter electrode connected to the gold current collectors on the cathode and anode sides. Prior to polarization, the cell was held at open-circuit voltage (OCV) for 2 min. Then, current densities of 50, 100, 150, and 200 mA cm^{-2} were applied for 30 min each. Voltage was measured continuously during each step, and the mean voltage over the final 30 seconds of each current density step was extracted for analysis as the "steady-state" voltage. All experiments were repeated in triplicate, and reported values represent mean ± standard deviation across replicates.

RESULTS AND DISCUSSION

Interposer Microstructural Analysis

Three-dimensional reconstructions obtained from X-ray tomography provide a volumetric view of the internal architecture of the two interposer materials. Attenuation contrast between the polymer matrix and voids enables the stacking of two-dimensional projection images into three-dimensional reconstructions suitable for geometric quantification (Figure 2a,b).[33,34] Image binarization further facilitates clear demarcation of the pore network (Figure 2c). Both PES and MES membranes exhibit a relatively uniform average porosity through the membrane thickness, with MES showing a local porosity of approximately 2% and PES exhibiting a local porosity of approximately 1.5% (Figure 2d). The PES interposer has a sponge-like morphology characterized by large, rounded, and poorly connected pores (Figure 2f; Figure 1). This pore structure is characterized by a broad pore-size distribution ranging from approximately 5 to 15 μm (Figure 2g). In contrast, the MCE interposer exhibits a higher density of smaller pores (Figure 2e) with a narrower pore size distribution centered around ∼5 μm and fewer large pores than PES.

XCT analysis reveals clear differences in the three-dimensional pore architectures of the MCE and PES interposers, which directly affect transport-relevant properties (Figure 3). Although both materials exhibit high porosity, MCE shows a slightly higher porosity (ε = 0.77) and lower tortuosity (τ = 1.58) than PES (ε = 0.71, τ = 1.64). This combination results in a lower MacMullin number for MCE (N_M = 2.05), indicating reduced resistance to through-plane transport. In contrast, the lower porosity and higher tortuosity of PES yield a larger MacMullin number (N_M = 2.33), reflecting increased pathway complexity consistent with its sponge-like morphology. Although PES has larger pores, its higher tortuosity and more hydrophobic polymer chemistry result in lower effective ionic conductivity than MCE. This comparison suggests that pore connectivity and topology, rather than porosity alone, play an important role in determining effective transport behavior. Overall, the XCT-derived metrics indicate that MCE provides more direct transport pathways and lower effective resistance than PES, highlighting the value of three-dimensional structural characterization for interposer evaluation.

https://doi.org/10.1021/acselectrochem.6c00038
ACS Electrochem. 2026, 2, 1304–1312

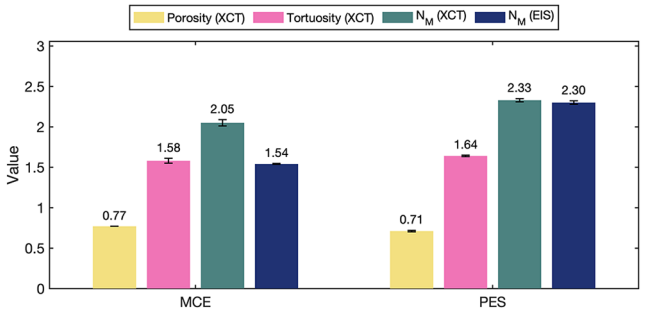

Figure 3. Tortuosity and MacMullin number of MCE and PES interposers measured using complementary techniques. Tortuosity was extracted from X-ray computed tomography (XCT), from which the MacMullin number (N_M) was calculated. The N_M was also independently determined via electrochemical impedance spectroscopy (EIS).

To verify whether these structural differences translate into measurable transport behavior, electrochemical impedance spectroscopy was used to quantify ionic transport through the interposers and independently determine their MacMullin numbers. Impedance measurements yield MacMullin numbers of 1.54 ± 0.0063 for MCE and 2.30 ± 0.015 for PES, in agreement with the trends observed from XCT. While the EIS-derived and XCT-derived MacMullin numbers differ in magnitude, both techniques consistently show reduced transport resistance for MCE relative to PES.

The MacMullin numbers obtained for the PES interposer are very similar between XCT (2.33) and EIS (2.30). In contrast, there is a larger discrepancy for the MCE interposer (XCT: 2.05; EIS: 1.54). The chemistry of the interposer is likely responsible for this difference, as the XCT analysis was performed on dry samples. In contrast, the electrochemical measurements were performed on interposers soaked in 1M KHO_3 solution. MCE is significantly more hydrophilic than PES and can absorb electrolyte when wetted. Cellulose-based membranes typically exhibit water uptake and swelling on the order of ∼10−30%, which can enhance pore wetting and connectivity within the porous structure.[35] This hydration effect can increase the effective ionic conductivity measured during EIS but would not be captured in the dry tomography images used for XCT analysis. In contrast, PES is more hydrophobic and typically exhibits minimal swelling (<3−5%), so hydration-induced changes in the pore structure are expected to be much less observed.[36]

Interposer Impact on CO_2 Electrolysis

Figure 4 summarizes the electrolyzer performance in terms of faradaic efficiencies for CO and H_2 as a function of current density for AgNP and Ni-SAC catalysts using three configurations: mixed cellulose ester (MCE), poly(ether sulfone) (PES), and a control (i.e., no interposer).

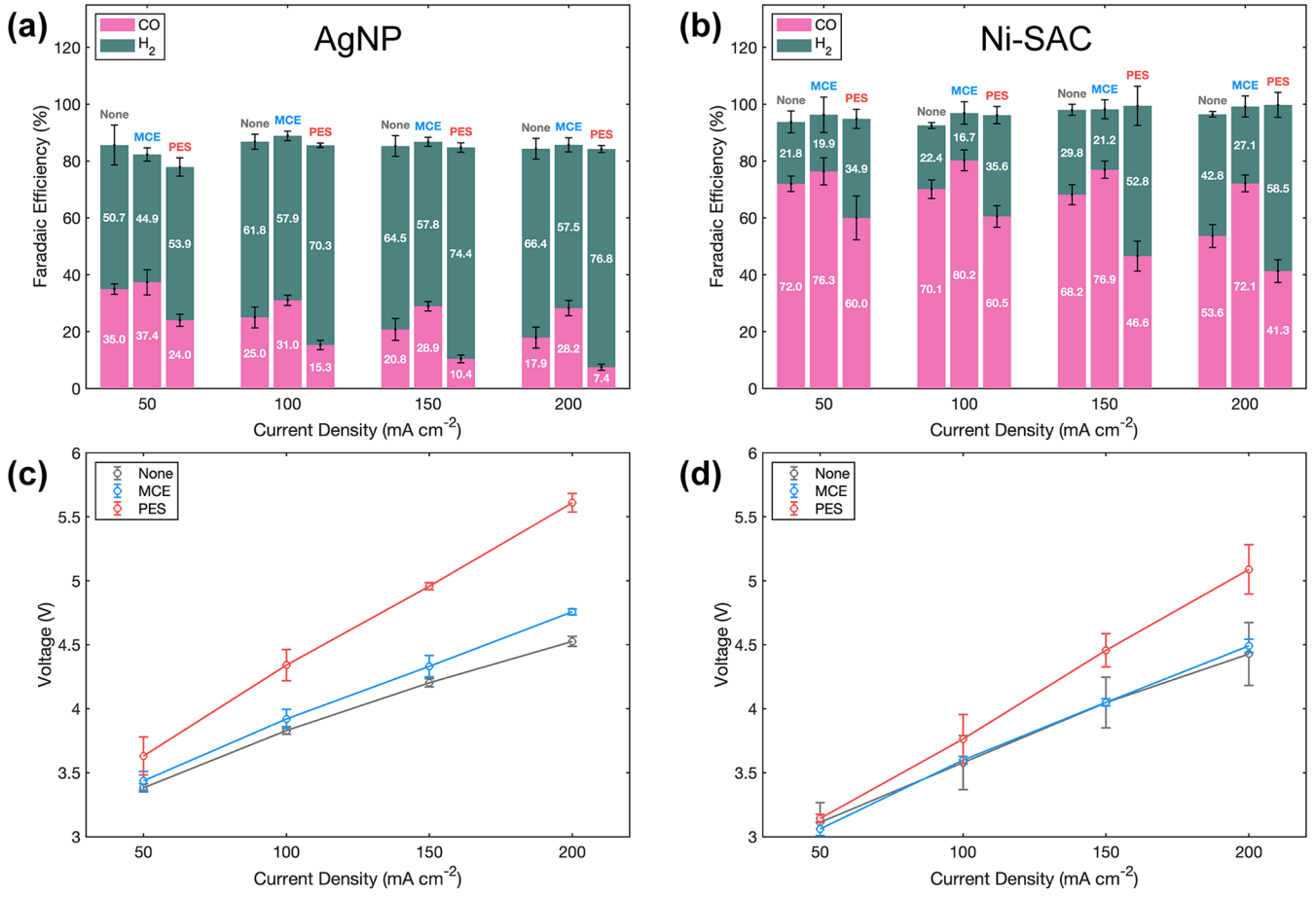

Figure 4. Faradaic efficiency of CO (pink) and H_2 (green) at four current densities (50−200 mA cm^{-2}) using the (a) Ag-NP catalyst and (b) Ni-SAC catalyst. Steady-state cell voltages using the (c) Ag-NP catalyst and (d) Ni-SAC catalyst, averaged over the final 30 s of each step. Error bars show standard deviations across replicates.

https://doi.org/10.1021/acselectrochem.6c00038
ACS Electrochem. 2026, 2, 1304−1312

In this architecture, the interposer serves both as an ionic transport medium and as a reactive zone where bicarbonate reactions can generate *in situ* CO_2 (*i*-CO_2). Consequently, the physical properties of the interposer play a central role in governing local reactant availability, pH gradients, and ultimately product selectivity. Previous studies of BPM-based CO_2 electrolysis have likewise shown that local ionic transport in the cathode-side porous region strongly governs the accessibility of regenerated CO_2 to catalytic sites, and that uneven transport can shift the local reaction environment toward HER.[37] In addition to through-plane transport, the porous interposer may also influence in-plane ion and gas transport, since pressure gradients and flow dispersion in electrochemical cells can drive convective transport within the plane of porous layers and thereby affect reactant distribution and electrochemical performance.[38]

The interposer layer also influences the spatial pH gradient between the BPM junction and the catalyst surface. Protons generated at the BPM react with bicarbonate within the interposer to form *in situ* CO_2, while hydroxide produced during electroreduction increases the alkalinity near the catalyst. As a result, the transport properties of the interposer define the region where these opposing fluxes meet and therefore influence both the local pH gradient and CO_2 availability at the catalyst surface. Previous studies have shown that the distance between the membrane and catalyst and the pore structure of the interposer can strongly influence local pH and CO_2 concentrations, as well as the formation of gas−liquid−catalyst triple-phase boundaries that enhance CO_2 reduction kinetics.[23] These effects are also expected to depend on current density because increasing current increases both proton and hydroxide fluxes in the system.

For both AgNP (Figure 4a) and Ni-SAC (Figure 4b), the MCE interposer consistently yields the highest CO faradaic efficiency across the range of current densities examined (50 to 200 mA cm^{-2}). In contrast, the PES interposer causes a substantial shift toward H_2 production at higher current densities, indicating that the highly porous structure of PES is less effective at sustaining favorable local conditions for CO_2 reduction. The pore network may not efficiently transport *in situ* CO_2 to the catalyst surface, reducing the formation of CO_2 reduction products. Literature reports that efficient electrolysis in BPM and carbonate-fed systems depends not only on generating *in situ* CO_2 at the membrane side interface, but also on transporting that regenerated CO_2 back through the porous layer fast enough for it to be consumed before it is lost to diffusion, recapture, or competing reactions.[39]

The improved electrolyzer performance of the MCE interposer is attributed to MCEs improved connectivity and lower MacMullin number. MCE's lower MacMullin number results in rapid replenishment of the reactant and minimal mass transfer limitations. The MCE interposer has a higher density of smaller pores compared to PES, resulting in a narrower pore-size distribution centered near 5 μm. This microstructure may increase electrolyte residence time within the interposer and reduce rapid bulk electrolyte exchange relative to PES. As a result, *in situ* generated CO_2 can remain near the catalyst interface for longer, helping sustain higher local CO_2 concentrations. Simultaneously, the lower MacMullin number reduces effective ionic resistance, allowing sufficient ionic conduction to sustain high current densities without excessive ohmic losses.

The interposer must balance two competing transport requirements. On one hand, high porosity and good pore connectivity promote efficient ionic transport and enable rapid delivery of *in situ* generated CO_2 to the catalyst. On the other hand, excessively large pores or high permeability can lead to rapid electrolyte exchange, which reduces residence time for CO_2 and can promote CO_2 recapture as bicarbonate. Consequently, optimal interposer design requires balancing transport flux with reactant residence time within the interphase.

Recent reactive-capture studies have found that as current density increases, the catalyst can become starved of *in situ* generated CO_2, causing a rapid decline in CO faradaic efficiency and a corresponding increase in competing hydrogen evolution.[23] Similarly, we found that at higher current densities, where direct CO_2 supply from the bulk electrolyte becomes increasingly limited, the ability of the interposer to generate and retain *in situ* CO_2 becomes critical. Prior studies have shown that local CO_2 availability governs faradaic efficiency trends and that porous interlayers with high porosity and connectivity enhance mass transport of *in situ* CO_2 and carbonate ions, thereby promoting multicarbon product formation and suppressing hydrogen evolution.[9,40] In systems using KHO_3 as the catholyte, CO_2 is generated locally at the acidic side of the bipolar membrane because of the reaction between the bicarbonate and protons

$$\text{In Interposer: } HCO_3^- + H^+ \rightleftharpoons CO_2 + H_2O \quad (4)$$

$$\text{At Catalyst: } CO_2 + 2H^+ + 2e^- \rightarrow CO + H_2O \quad (5)$$

$$2H_2O + 2e^- \rightarrow H_2 + 2OH^- \quad (6)$$

Increasing KHO_3 concentration can further influence this process by increasing the availability of bicarbonate for proton-driven *in situ* CO_2 generation at the bipolar membrane interface, which has been reported to increase CO faradaic efficiency in bicarbonate electrolyzers at higher electrolyte concentrations.[11] The MCE interposer appears to effectively buffer local CO_2 availability by coupling hydroxide transport with carbonate neutralization reactions, thereby mitigating CO_2 recapture and suppressing competitive hydrogen evolution. The broader pore size distribution and larger pores in PES likely increase electrolyte permeability and reduce the residence time of *in situ* CO_2 within the interposer region. This can increase the probability of CO_2 reacting with hydroxide in the bulk electrolyte and being recaptured as bicarbonate before reaching the catalyst.

The voltage−current relationships provide insights into the energy consumed for each system (Figure 4c,d). For the AgNP catalyst, the use of the MCE interposer results in only a modest increase in cell voltage, ranging from 0.05 to 0.23 V across current densities of 50−200 mA cm^{-2}, when compared with an electrolyzer without a interposer layer. Since the interposer is a non-conductive layer with a ohmic resistance this increase is expected. However, the PES interposer imposes a substantially larger voltage penalty of 0.25−1.08 V. This voltage increase is linked to the transport resistance. In the case of Ni-SAC, the MCE interposer is effectively voltage-neutral, with voltage differences that are within or comparable to the experimental standard deviation, while PES again leads to a noticeable increase in cell voltage (0.03−0.66 V). The Ni-SAC consistently operates at lower absolute voltages than AgNP for a given interposer due to its improved reaction kinetics.

https://doi.org/10.1021/acselectrochem.6c00038
ACS Electrochem. 2026, 2, 1304−1312

However, the relative voltage trends induced by interposer selection remain consistent across both catalysts.

These results show that using an MCE interposer improves the product selectivity and energy efficiency of the electrolyzer when compared with the PES. The voltage profile is directly linked to the difference in mass transport through the interposers. While the improved CO selectivity observed with MCE indicates that the MCE allows reduced CO_2 recapture and more rapid transport of CO_2 across the interphase between the cathode and the BPM. This promotes a more ideal local reaction environment. Importantly, the combination of higher porosity and lower MacMullin number in MCE enables efficient ionic conduction while maintaining favorable conditions for *in situ* CO_2 generation.

These trends are consistent with the work of Lee et al., who explored several materials and found that a higher-porosity (>80%) interposer with pores >3 μm boosted C_2^+ product selectivity by accelerating mass transport of both *in situ*-CO_2 gas and carbonate ions across the interposer layer.[9] The higher porosity means a larger fraction of interposer volume is open, with more space to be filled with electrolyte and facilitate transport. The MCE interposer creates more diffusion pathways, raising the local CO_2 concentration at the catalyst layer. In our work, MCE combines greater porosity ($\varepsilon \approx 0.77$) with a highly connected network (lower N_M), which facilitates faster CO_2 and ion diffusion, stabilizes the local pH, and suppresses the hydrogen evolution reaction (HER). The poorly connected, lower-porosity PES membrane instead restricts these fluxes, leading to CO_2 starvation and the sharp decline in CO selectivity observed here.

In addition to these structural differences, the intrinsic wettability of the interposer materials may also influence electrolyte distribution and transport. In battery separator research, the hydrophilicity of cellulose has been shown to significantly improve electrolyte wettability and ionic conductivity.[41] Cellulose-based membranes have a strong affinity for water due to their abundant polar hydroxyl groups. Their fine, interconnected pore network can also act as a wick, drawing electrolyte into pores and toward the BPM interface. In contrast, PES is more hydrophobic, which may lead to incomplete wetting and the formation of gas bubbles that displace liquid within the pore network. Poor wetting at the BPM/cathode interface increases membrane resistance and can shift the reaction toward hydrogen evolution.[42]

Lastly, interposer thickness also influences electrochemical performance. The PES interposer is significantly thicker (102.07 μm) than the MCE interposer (71.11 μm), which can exacerbate mass-transport limitations. Because permeability scales inversely with material thickness, the greater thickness of PES is expected to hinder diffusive transport and contribute to increased ionic resistance, consistent with the higher cell voltages observed. Reducing interposer thickness would shorten the ionic transport path length and lower ohmic losses, thereby decreasing the overall cell voltage. However, excessive thinning may compromise the stability and effectiveness of *in situ* CO_2 generation within the interposer by reducing reactant residence time and limiting carbonate neutralization. As demonstrated extensively in gas-phase electrolysis and fuel cell systems, careful membrane–electrode architecture design is critical for balancing transport, reaction, and stability. These considerations are equally important in liquid-phase electrolysis, where improper design can lead to reactant depletion, concentration gradients, and salt precipitation that degrade performance.

CONCLUSION

This work establishes a connection between porous interposer microstructure and the performance of integrated BPM CO_2 electrolyzers, and highlights the utility of non-dimensional transport metrics for interposer design. X-ray tomography and symmetric-cell impedance measurements show that mixed cellulose ester (MCE) exhibits a lower MacMullin number (N_M = 2.05 from XCT and 1.54 from EIS) than poly(ether sulfone) (PES) ($N_M \approx 2.3$), indicating shorter effective ionic pathways and reduced tortuosity. When implemented in a membrane–electrode assembly, the lower N_M of MCE enables more effective *in situ* CO_2 generation and retention near the catalyst, resulting in higher CO faradaic efficiencies and lower cell voltages (improved energy efficiency) across 50–200 mA cm^{-2}. These results demonstrate that non-dimensional descriptors such as the MacMullin number provide a powerful, materials-agnostic framework for rationally designing interposers that enhance *in situ* CO_2 availability and suppress competing hydrogen evolution in BPM CO_2 electrolysis.

ASSOCIATED CONTENT

Supporting Information

The Supporting Information is available free of charge at https://pubs.acs.org/doi/10.1021/acselectrochem.6c00038.

SEM images of MCE and PES interposers at multiple magnifications; Nyquist plots and extracted resistances from symmetric-cell EIS measurements used to determine MacMullin number; structural and transport parameters used to calculate effective ionic conductivity; and porosity, tortuosity, and MacMullin number determined from X-ray computed tomography analysis (PDF)

AUTHOR INFORMATION

Corresponding Authors

Marta C. Hatzell − *George W. Woodruff School of Mechanical Engineering, Georgia Institute of Technology, Atlanta, Georgia 30332, United States; School of Chemical and Biomolecular Engineering, Georgia Institute of Technology, Atlanta, Georgia 30332, United States;* orcid.org/0000-0002-5144-4969; Email: marta.hatzell@me.gatech.edu

Kelsey B. Hatzell − *Andlinger Center for Energy and the Environment, Princeton, New Jersey 08540, United States; Department of Mechanical and Aerospace Engineering, Princeton University, Princeton, New Jersey 08540, United States; Department of Chemical and Biological Engineering, Princeton University, Princeton, New Jersey 08540, United States;* orcid.org/0000-0002-5222-7288; Email: kelsey.hatzell@princeton.edu

Authors

Elizabeth Dentzer − *Andlinger Center for Energy and the Environment, Princeton, New Jersey 08540, United States; Department of Mechanical and Aerospace Engineering, Princeton University, Princeton, New Jersey 08540, United States*

Hanwoong Kim − *George W. Woodruff School of Mechanical Engineering, Georgia Institute of Technology, Atlanta,*

Georgia 30332, United States; orcid.org/0009-0003-0828-0123

Yaguang Zhu − *Andlinger Center for Energy and the Environment, Princeton, New Jersey 08540, United States;* orcid.org/0000-0002-1522-4491

Hakhyeon Song − *George W. Woodruff School of Mechanical Engineering, Georgia Institute of Technology, Atlanta, Georgia 30332, United States;* orcid.org/0000-0003-2343-2212

Nicole Callen − *Andlinger Center for Energy and the Environment, Princeton, New Jersey 08540, United States*

Claudio A. Ruiz Torres − *Andlinger Center for Energy and the Environment, Princeton, New Jersey 08540, United States;* orcid.org/0000-0001-5183-4791

Hyeonuk Choi − *Department of Materials Science and Engineering, Korea Advanced Institute of Science and Technology (KAIST), Daejeon 34141, Republic of Korea;* orcid.org/0000-0001-6798-1999

Jihun Oh − *Department of Materials Science and Engineering, Korea Advanced Institute of Science and Technology (KAIST), Daejeon 34141, Republic of Korea;* orcid.org/0000-0001-6465-6736

Complete contact information is available at: https://pubs.acs.org/10.1021/acselectrochem.6c00038

Notes

The authors used AI-assisted tools to help generate MATLAB code for data visualization. The authors reviewed and verified all outputs.

The authors declare no competing financial interest.

■ ACKNOWLEDGMENTS

This work was funded by the Advanced Research Projects Agency−Energy (ARPA-E), U.S. Department of Energy, under Award Number DE-AR0001949. J.O. and H.C. were supported by the National Research Foundation of Korea (NRF) grant funded by the Korea government (MSIT) (No. RS-2021-NR060090) for catalyst synthesis.

■ REFERENCES

(1) Lindsey, R. Climate change: atmospheric carbon dioxide NOAA Climate.gov 2025 https://www.climate.gov/news-features/understanding-climate/climate-change-atmospheric-carbon-dioxide

(2) Do, T. N.; You, C.; Kim, J. A CO 2 utilization framework for liquid fuels and chemical production: techno-economic and environmental analysis. *Energy Environ. Sci.* **2022**, *15*, 169−184.

(3) Song, H.; Fernández, C. A.; Venkataraman, A.; Brandão, V. D.; Dhingra, S. S.; Arora, S. S.; Bhargava, S. S.; Villa, C. M.; Sievers, C.; Nair, S.; Hatzell, M. C. Ethylene Production from Carbonate Using a Bipolar Membrane Electrolysis System. *ACS Appl. Energy Mater.* **2024**, *7*, 1224−1233.

(4) Venkataraman, A.; Song, H.; Brandão, V. D.; Ma, C.; Casajus, M. S.; Fernandez Otero, C. A.; Sievers, C.; Hatzell, M. C.; Bhargava, S. S.; Arora, S. S.; et al. Process and techno-economic analyses of ethylene production by electrochemical reduction of aqueous alkaline carbonates. *Nat. Chem. Eng.* **2024**, *1*, 710−723.

(5) Rabinowitz, J. A.; Kanan, M. W. The future of low-temperature carbon dioxide electrolysis depends on solving one basic problem. *Nat. Commun.* **2020**, *11*, No. 5231.

(6) Brandão, V. D.; Song, H.; Venkataraman, A.; Fishler, Y.; Arora, S. S.; Bhargava, S. S.; Villa, C.; Holewinski, A.; Nair, S.; Hatzell, M. C. Temperature Effects on the Surface CO Population during CO2 Electroreduction over Copper. *ACS Catal.* **2025**, *15*, 8979−8990.

(7) Abbaszadeh, M.; Garell, M.; Choi, J. I.; Chen, Y.; Leisen, J.; Jang, S. S.; Hu, Y.-Y.; Hatzell, M. C. Unraveling water and salt transport in polyamide with nuclear magnetic resonance spectroscopy. *ACS Mater. Lett.* **2023**, *5*, 291−298.

(8) Fink, A. G.; Lees, E. W.; Zhang, Z.; Ren, S.; Delima, R. S.; Berlinguette, C. P. Impact of alkali cation identity on the conversion of HCO3- to CO in bicarbonate electrolyzers. *ChemElectroChem* **2021**, *8*, 2094−2100.

(9) Lee, G.; Rasouli, A. S.; Lee, B. H.; et al. CO2 electroreduction to multicarbon products from carbonate capture liquid. *Joule* **2023**, *7*, 1277−1288, DOI: 10.1016/j.joule.2023.05.003.

(10) Song, H.; Fernández, C. A.; Choi, H.; Huang, P.-W.; Oh, J.; Hatzell, M. C. Integrated carbon capture and CO production from bicarbonates through bipolar membrane electrolysis. *Energy Environ. Sci.* **2024**, *17*, 3570−3579.

(11) Li, T.; Lees, E. W.; Goldman, M.; Salvatore, D. A.; Weekes, D. M.; Berlinguette, C. P. Electrolytic conversion of bicarbonate into CO in a flow cell. *Joule* **2019**, *3*, 1487−1497.

(12) Song, H.; Fernandez, C.; Venkataraman, A.; Brandao, V.; Dhingra, S.; Arora, S. S.; Villa, C.; Ferrari, D.; Sievers, C.; Nair, S.; Hatzell, M. CO2 Capture and Conversion to Ethylene using a Bipolar Membrane Electrolysis System 2023 https://chemrxiv.org/engage/chemrxiv/article-details/64e117a3694bf1540ca2e3b5.

(13) Lees, E. W.; Goldman, M.; Fink, A. G.; Dvorak, D. J.; Salvatore, D. A.; Zhang, Z.; Loo, N. W.; Berlinguette, C. P. Electrodes designed for converting bicarbonate into CO. *ACS Energy Lett.* **2020**, *5*, 2165−2173.

(14) Brandão, V. D.; Long, O.; Zhong, S.; Fushio, R.; Venkataraman, A.; Song, H.; Hatzell, M. C.; Nair, S.; Sievers, C. Local pH Effects on the Temperature Dependence of Product Formation in CO2 Electrolyzers. *J. Am. Chem. Soc.* **2026**, *148*, 2801 DOI: 10.1021/jacs.5c20444.

(15) Hatzell, M. C.; Zhu, X.; Logan, B. E. Simultaneous hydrogen generation and waste acid neutralization in a reverse electrodialysis system. *ACS Sustainable Chem. Eng.* **2014**, *2*, 2211−2216.

(16) Shehzad, M. A.; Yasmin, A.; Ge, X.; Ge, Z.; Zhang, K.; Liang, X.; Zhang, J.; Li, G.; Xiao, X.; Jiang, B.; Wu, L.; Xu, T. Shielded goethite catalyst that enables fast water dissociation in bipolar membranes. *Nat. Commun.* **2021**, *12*, No. 9.

(17) Larrea, C.; Avilés-Moreno, J. R.; Ocón, P. Strategies to Enhance CO2 Electrochemical Reduction from Reactive Carbon Solutions. *Molecules* **2023**, *28*, No. 1951, DOI: 10.3390/molecules28041951.

(18) Hatzell, M. C.; Logan, B. E. Evaluation of flow fields on bubble removal and system performance in an ammonium bicarbonate reverse electrodialysis stack. *J. Membr. Sci.* **2013**, *446*, 449−455.

(19) Bui, J. C.; Lucas, É.; Lees, E. W.; Liu, A. K.; Atwater, H. A.; Xiang, C.; Bell, A. T.; Weber, A. Z. Analysis of bipolar membranes for electrochemical CO2 capture from air and oceanwater. *Energy Environ. Sci.* **2023**, *16*, 5076−5095, DOI: 10.1039/D3EE01606D.

(20) Lees, E. W.; Bui, J. C.; Song, D.; Weber, A. Z.; Berlinguette, C. P. Continuum model to define the chemistry and mass transfer in a bicarbonate electrolyzer. *ACS Energy Lett.* **2022**, *7*, 834−842.

(21) Zhang, G.; Ye, K.; Ni, B.; Jiang, K. Steering the products distribution of CO2 electrolysis: A perspective on extrinsic tuning knobs. *Chem. Catal.* **2023**, *3*, No. 100746.

(22) Blommaert, M. A.; Sharifian, R.; Shah, N. U.; Nesbitt, N. T.; Smith, W. A.; Vermaas, D. A. Orientation of a bipolar membrane determines the dominant ion and carbonic species transport in membrane electrode assemblies for CO2 reduction. *J. Mater. Chem. A* **2021**, *9*, 11179−11186, DOI: 10.1039/D0TA12398F.

(23) Liu, H.; Shin, H.; Li, X.-Y.; Su, G.; Ou, P.; Wang, Y.; Chen, L.; Yu, J.; Chen, Y.; Xia, R.; et al. Hierarchically porous carbon supports enable efficient syngas production in electrified reactive capture. *Energy Environ. Sci.* **2025**, *18*, 6628 DOI: 10.1039/D5EE00094G.

(24) Lee, G.; Rasouli, A. S.; Lee, B.-H.; Zhang, J.; Won, D. H.; Xiao, Y. C.; Edwards, J. P.; Lee, M. G.; Jung, E. D.; Arabyarmohammadi, F.; et al. CO2 electroreduction to multicarbon products from carbonate capture liquid. *Joule* **2023**, *7*, 1277−1288.

(25) Liu, H.; An, L.; Wang, P.; Yu, C.; Zhang, J.; Shin, H.; Peng, B.; Li, J.; Li, M.; An, H.; et al. Interconnected nanoconfining pore networks enhance catalyst CO2 interaction in electrified reactive capture. *Nat. Commun.* **2025**, *16*, No. 6185.
(26) Martínez-Rodríguez, M. J.; Cui, T.; Shimpalee, S.; Seraphin, S.; Duong, B.; Van Zee, J. W. Effect of microporous layer on MacMullin number of carbon paper gas diffusion layer. *J. Power Sources* **2012**, *207*, 91−100.
(27) Raccichini, R.; Furness, L.; Dibden, J. W.; Owen, J. R.; García-Araez, N. Impedance Characterization of the Transport Properties of Electrolytes Contained within Porous Electrodes and Separators Useful for Li-S Batteries. *J. Electrochem. Soc.* **2018**, *165*, A2741.
(28) Dixit, M. B.; Moreno, D.; Xiao, X.; Hatzell, M. C.; Hatzell, K. B. Mapping charge percolation in flowable electrodes used in capacitive deionization. *ACS Mater. Lett.* **2019**, *1*, 71−76.
(29) Lin, L.; Ayyaswamy, A.; Zheng, Y.; Fan, A.; Vishnugopi, B. S.; Mukherjee, P. P.; Hatzell, K. B. Nonintuitive role of solid electrolyte porosity on failure. *ACS Energy Lett.* **2024**, *9*, 2387−2393.
(30) Zheng, Y.; Hatzell, K. B. Ultrasparse view X-ray computed tomography for 4D imaging. *ACS Appl. Mater. Interfaces* **2023**, *15*, 35024−35033.
(31) Landesfeind, J.; Hattendorff, J.; Ehrl, A.; Wall, W. A.; Gasteiger, H. A. Tortuosity Determination of Battery Electrodes and Separators by Impedance Spectroscopy. *J. Electrochem. Soc.* **2016**, *163*, A1373.
(32) Zhang, J.; Hatzell, K. B.; Hatzell, M. C. A combined heat-and power-driven membrane capacitive deionization system. *Environ. Sci. Technol. Lett.* **2017**, *4*, 470−474.
(33) Ventura-Martinez, K.; Zhu, Y.; Booth, A.; Hatzell, K. B. Impact of Asymmetric Microstructure on Ion Transport in Ti3C2T x Membranes. *Nano Lett.* **2024**, *24*, 13551−13557.
(34) Dixit, M. B.; Zaman, W.; Bootwala, Y.; Zheng, Y.; Hatzell, M. C.; Hatzell, K. B. Scalable manufacturing of hybrid solid electrolytes with interface control. *ACS Appl. Mater. Interfaces* **2019**, *11*, 45087−45097.
(35) Etale, A.; Onyianta, A. J.; Turner, S. R.; Eichhorn, S. J. Cellulose: A Review of Water Interactions, Applications in Composites, and Water Treatment. *Chem. Rev.* **2023**, *123*, 2016−2048, DOI: 10.1021/acs.chemrev.2c00477.
(36) Susanto, H.; Ulbricht, M. Characteristics, performance and stability of polyethersulfone ultrafiltration membranes prepared by phase separation method using different macromolecular additives. *J. Membr. Sci.* **2009**, *327*, 125−135, DOI: 10.1016/j.memsci.2008.11.025.
(37) Li, M.; Lees, E. W.; Ju, W.; Subramanian, S.; Yang, K.; Bui, J. C.; Iglesias van Montfort, H.-P.; Abdinejad, M.; Middelkoop, J.; Strasser, P.; Weber, A. Z.; Bell, A. T.; Burdyny, T. Local ionic transport enables selective PGM-free bipolar membrane electrode assembly *Nat. Commun.*, *15* 8222 .
(38) Gostick, J. T.; Fowler, M. W.; Pritzker, M. D.; Ioannidis, M. A.; Behra, L. M. In-plane and through-plane gas permeability of carbon fiber electrode backing layers. *J. Power Sources* **2006**, *162*, 228−238.
(39) Xie, K.; Miao, R. K.; Ozden, A.; Liu, S.; Chen, Z.; Dinh, C.-T.; Huang, J. E.; Xu, Q.; Gabardo, C. M.; Lee, G.; Edwards, J. P.; O'Brien, C. P.; Boettcher, S. W.; Sinton, D.; Sargent, E. H. Bipolar membrane electrolyzers enable high single-pass CO2 electroreduction to multicarbon products. *Nat. Commun.* **2022**, *13*, 3609 DOI: 10.1038/s41467-022-31295-3.
(40) Liu, H.; An, L.; Wang, P.; et al. Interconnected nanoconfining pore networks enhance catalyst CO2 interaction in electrified reactive capture. *Nat. Commun.* **2025**, *16*, 6185 DOI: 10.1038/s41467-025-61407-8.
(41) Zhao, T.; Xiao, P.; Luo, M.; Nie, S.; Li, F.; Liu, Y. Eco-Friendly Lithium Separators: A Frontier Exploration of Cellulose-Based Materials. *Int. J. Mol. Sci.* **2024**, *25*, No. 6822.
(42) Dessiex, M.; Fischer, R.; Weng, T.-W.; Marone, F.; Binder, B.; Lunati, I.; Haussener, S.; Büchi, F. N. Water Management in Zero-Gap CO2 Electrolyzer with Forward Bias Bipolar Membranes. *J. Electrochem. Soc.* **2025**, *172*, No. 054504.

https://doi.org/10.1021/acselectrochem.6c00038
ACS Electrochem. 2026, 2, 1304−1312